ORNL/SPR-2021/1838
Rev. 0

HFIR SiC Bowing Test Ready to Insert

Nuclear Technology Research and Development

**Approved for public release.
Distribution is unlimited.**

Prepared for
U.S. Department of Energy
Nuclear Technology R&D Program
Advanced Fuels Campaign

Authors:
Christian M. Petrie, Josina W. Geringer, Adam James, Kurt Smith, Joseph R. Burns, Annabelle G. Le Coq, Nicholas Russell, Christian P. Deck, Takaaki Koyanagi, Yutai Katoh
Oak Ridge National Laboratory

March 2021
M2FT-21OR020203041

ACKNOWLEDGEMENTS

This research was sponsored by the Advanced Fuels Campaign (AFC) Program of the US Department of Energy (DOE), Office of Nuclear Energy. Neutron irradiation in the High Flux Isotope Reactor (HFIR) is made possible by the Office of Basic Energy Sciences, US DOE. The report was authored by UT-Battelle under Contract No. DE-AC05-00OR22725 with US DOE. David Bryant (Oak Ridge National Laboratory) performed the specimen engraving and experiment assembly. Nathan Capps and Jacob Gorton (Oak Ridge National Laboratory) performed technical reviews of the report and provided helpful comments. Maureen Searles (Oak Ridge National Laboratory) performed the HFIR safety review and wrote the experiment authorization basis document.

SUMMARY

This report describes the successful assembly of a High Flux Isotope Reactor (HFIR) irradiation experiment designed to assess radiation-induced lateral bowing of silicon carbide fiber–reinforced, silicon carbide matrix composite (SiC/SiC) components under a radial fast neutron flux gradient. Excessive bowing of a SiC/SiC channel box in a boiling water reactor could potentially interfere with control blade movements. Similar concerns exist for SiC/SiC fuel cladding in light water reactors. The experiment described herein will provide experimental validation of the structural response of a miniature SiC/SiC channel box and tube specimens with pressurized water reactor diameters during irradiation. The significant radial fast neutron flux gradients that exist in the permanent reflector of HFIR were characterized using detailed three-dimensional neutronic calculations. The three-dimensional displacement damage dose rate profile and the resulting volumetric swelling in SiC were used as inputs to structural analyses that predicted the deformation and stresses in the channel box specimen. The specimens were thoroughly characterized prior to irradiation using traditional dimensional inspection and surface profilometry so that these measurements can later be compared with similar measurements that will be made post-irradiation to determine radiation-induced deformations. Furthermore, fine engraving markers were inscribed along all outer surfaces of the specimen and mapped using a digital microscope and a three-dimensional stage. This technique allowed for accurate measurements of the marker spacings, which can be compared with similar measurements that will be made post-irradiation to provide local radiation-induced strain mapping. The experiment was successfully assembled and is scheduled for insertion during HFIR cycle 492, which is currently scheduled to run from May 25, 2021 to June 18, 2021.

CONTENTS

FIGURES

TABLES

HFIR SiC BOWING TEST READY TO INSERT

1. INTRODUCTION

Silicon carbide (SiC) fiber–reinforced, SiC ceramic matrix composites (SiC/SiC composites) have long been considered for use in a wide range of nuclear applications [1] because of their high strength [2, 3] and dimensional stability [4, 5] under irradiation and at high temperatures, and their minimal neutron absorption [6]. These materials also exhibit superior oxidation kinetics in steam and air environments compared with most metal alloys and other high-temperature materials such as graphite [7, 8]. These characteristics make SiC/SiC composites attractive both for advanced high-temperature reactors [9] and for improved accident tolerance in light water reactors (LWRs) [10-12]. One of the primary benefits associated with SiC/SiC composites and other accident-tolerant fuels (ATFs) is the mitigation of significant heating and hydrogen generation caused by exothermic steam oxidation reactions with zirconium (Zr) -based fuel cladding during severe accidents, particularly beyond design basis accidents [13].

The international effort to deploy ATFs has gained much attention over the past decade, and SiC/SiC composite fuel cladding remains an attractive option if concerns related to hydrothermal corrosion [14-16] and fission product retention during irradiation with significant thermal gradients [17-22] can be resolved. In addition to fuel cladding, the accident tolerance of other core internal structures has been considered as a part of a broader effort to reduce the mass of Zr in LWRs to ultimately mitigate the consequences of severe accidents and allow more time for operator intervention [23]. Although all core internal structures must demonstrate acceptable corrosion rates, the requirements for maintaining hermeticity may not be as stringent for many in-core components. Examples of SiC/SiC components that could replace current Zr components include channel boxes in boiling water reactors (BWRs) and control rod and instrument guide tubes in pressurized water reactors (PWRs). BWR channel boxes provide structure to the core and prevent hydraulic communication between adjacent channels [24].

Other than hydrothermal corrosion issues, the primary concern for SiC/SiC composite core internal structures is radiation-induced lateral bowing [23]. Bowing is a concern even for current Zr-based channel boxes because any distortion of the channel box could obstruct coolant flow or interfere with control blade movements. The mechanism driving lateral bowing of SiC/SiC composite structures is differential neutron radiation swelling of SiC in the presence of fast neutron flux gradients. Neutron radiation swelling of SiC, and its temperature and dose dependence, are well characterized [1, 4, 25], particularly in the point defect swelling regime (~200–1,000°C) that spans the range of interest for LWR applications. Figure 1 shows a schematic (not to scale) of four BWR channel boxes surrounding a single control blade. Figure 1 also illustrates how a gradient in fast neutron flux (φ_{fast}) results in differential neutron swelling across the channel box, causing lateral bowing. Gradients would be expected to be more significant for fuel assemblies located near the periphery of the core, but significant gradients could exist elsewhere, depending on the distributions of burnup and enrichment within the core.

Figure 2a shows a model [4] for radiation-induced swelling of SiC as a function of dose in displacements per atom, or dpa. Differential swelling is caused by spatial variations in dose (or fast neutron fluence) or temperature. In the former case, the difference in dose on two opposite faces of a component increases linearly as a function of time. This causes the differential swelling to increase until the swelling starts to saturate on the face with the higher dose rate; eventually, the swelling on the opposite face catches up and the differential swelling approaches zero. Differential swelling is plotted in Figure 2b as a function of time in a BWR assuming a maximum dose rate of 4 dpa/year at a constant temperature (300°C) with the variation in fast neutron flux $\Delta\varphi_{fast}$ across the channel box as a parameter. Using small-angle approximations and assuming isotropic swelling, it can be shown that the geometric relationship between the maximum lateral

bowing Δx_{max} of a channel box—with length L and cross-sectional width W—and the differential swelling $\left(\frac{dV}{V}\right)_{diff}$ is

$$\Delta x_{max} = \frac{L^2\left(\frac{dV}{V}\right)_{diff}}{24W}, \quad (1)$$

with a maximum radius of curvature (R) equal to

$$R = \frac{3W}{\left(\frac{dV}{V}\right)_{diff}}. \quad (2)$$

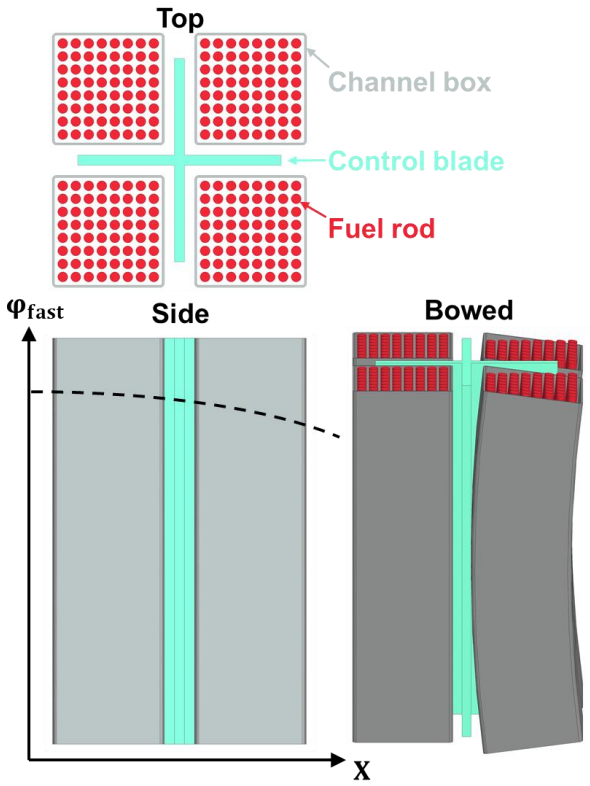

Figure 1. Illustration (not to scale) of BWR channel box showing how a gradient in fast neutron flux (φ_{fast}) in the X direction results in differential neutron swelling across the channel box, causing lateral bowing. Bowing could obstruct coolant flow or interfere with control blade movements.

In addition to the differential swelling, Figure 2b shows the bowing for a BWR channel box calculated using Eq. (1) assuming L=3,800 mm and W=140 mm [23]. Figure 2b shows that unconstrained differential swelling could cause lateral bowing that exceeds the allowable bowing of approximately 5 mm within ~10 days of operation if $\Delta\varphi_{fast}$ is greater than ~20%. According to Yueh et al, about a dozen fresh channels experience flux gradients between 25 and 29% [23]. While spatial gradients in fast neutron flux may cause temporary bowing of a BWR channel box, spatial variations in temperature across the width of a channel box can result in permanent bowing due to differential swelling that exists even after saturation (see Figure 2a). Figure 2c shows the differential swelling and resulting channel bow as a function of irradiation time and dose with the temperature difference across the channel ΔT as a parameter. Figure 2c shows that even for relatively large temperature variations of up to 15°C, the resulting lateral bowing is less than 3 mm. For comparison, high-fidelity thermal hydraulic simulations predict the ΔT will be closer to 2.5°C [26].

Therefore, spatial variations in neutron flux are expected to be more likely to result in significant channel box bowing than spatial variations in temperature. Previous work has shown that circumferential temperature variations in SiC/SiC fuel cladding of up to 8% can result in lateral bowing of 6.2 mm [27].

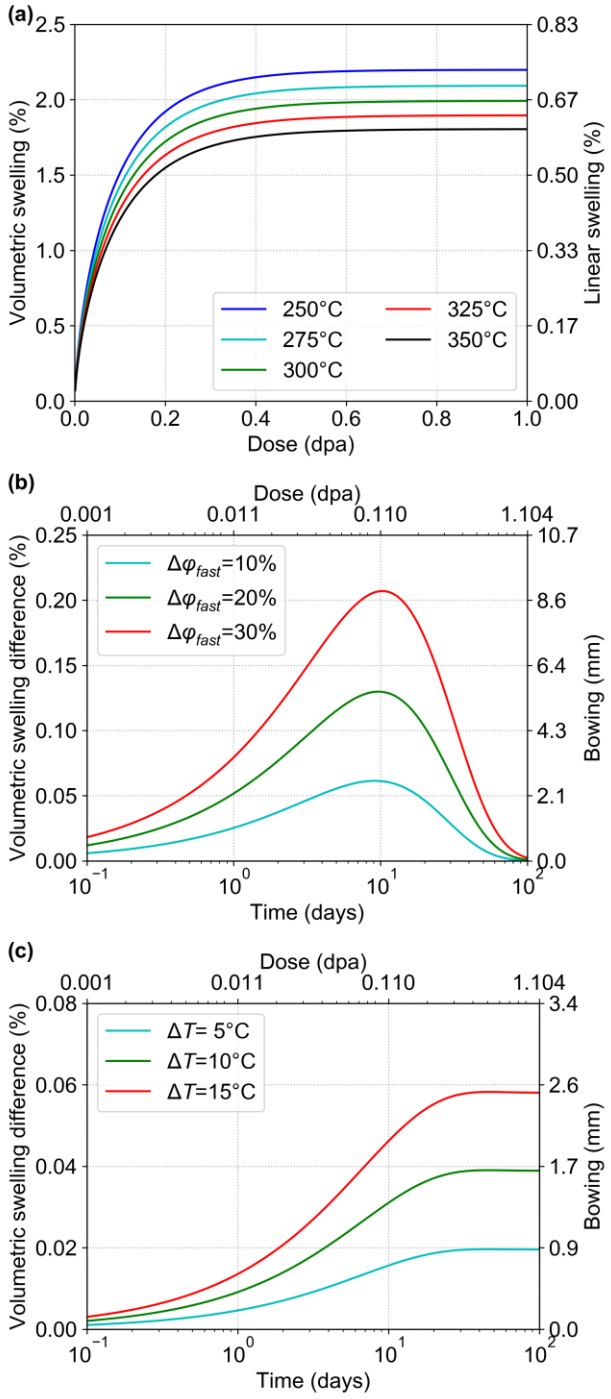

Figure 2. (a) Temperature- and dose-dependent volumetric and linear swelling of SiC [4]; (b) differential volumetric swelling and resulting lateral bowing vs. time and dose for various fast neutron flux gradients ($\Delta\varphi_{fast}$) across the width of a channel box; (c) differential volumetric swelling and resulting lateral bowing vs. time and dose for various temperature gradients (ΔT) across the width of a channel box.

Although this simplistic approach provides reasonable estimates for the expected channel box bowing and its dependence on temperature, dose, and spatial variations in both parameters, there are several factors that it does not consider. This approach ignores the effects of the channel box's stiffness, mechanical constraints imposed by the fuel rods and surrounding structural materials, and other phenomena such as matrix microcracking and irradiation creep. Recently, high-fidelity finite element analyses (FEAs) have been performed to asses bowing of a SiC/SiC channel box with representative thermal-hydraulic, neutronic, and structural boundary conditions [26]. However, to date, there have been no experimental data to validate the thermomechanical models. This work describes an irradiation experiment to measure the lateral bowing of a miniature SiC/SiC channel box that was fabricated by General Atomics (GA). The channel box will be irradiated in the reflector of the High Flux Isotope Reactor (HFIR) at Oak Ridge National Laboratory (ORNL). In the reflector positions, there exist significant radial fast neutron flux gradients to drive a swelling differential. The results of this experiment will be used to improve the understanding of unconstrained SiC/SiC deformation and validate thermomechanical models that can simulate bowing with and without the effects of mechanical constraints imposed by the fuel and surrounding structural components. The irradiation will also be conducted at HFIR coolant temperatures (50−60°C), as opposed to typical BWR temperatures. This approach prevents the need to perform a complex experiment that includes representative temperatures, dose rate distributions, and mechanical constraints. This report describes the design of the irradiation experiment, pre-irradiation characterization, and successful assembly.

2. EXPERIMENT DESIGN

The channel box bowing experiment is being performed in the permanent reflector of HFIR, which is a beryllium-reflected, pressurized, light water–cooled and moderated flux trap–type reactor [28, 29]. The channel box experiment will be irradiated in a large Vertical Experiment Facility (VXF) in the HFIR reflector. The reflector effectively thermalizes neutrons that leak from HFIR's core, resulting in significant radial gradients in the fast neutron flux, conditions ideal for driving bowing due to differential radiation swelling. The experiment design allows for a miniature channel box specimen and two tube specimens to be directly exposed to the reactor coolant, which flows through the experiment from top to bottom at a temperature in the range of 50−60°C. Pre-irradiation characterization of these specimens is covered by a separate programmatic activity and will therefore be documented in a separate report. All specimens will be irradiated for up to two HFIR cycles, which are each approximately 25 days in duration.

The irradiation experiment design is shown in Figure 3. The irradiation vehicle is a two-piece aluminum holder that, when welded together, results in a cylindrical assembly with internal cutouts for the specimens. The orifice at the bottom of the holder controls the coolant flow rate that enters from the top of the experiment. The miniature channel box and tube specimens are assembled inside of the holder cutout. The nominal dimensions of the miniature channel box are 30 mm × 30 mm × 380 mm, with a 1.25 mm wall thickness. The tube specimens have a prototypic PWR cladding diameter of 9.5 mm, a wall thickness of ~1 mm, and a length of 380 mm. Two aluminum internal supports, lower and upper, are stacked together on either end of the channel box and secured using a tie rod. The large features at the top and bottom of the support pieces ensure that the channel box remains centered inside the aluminum holder. Wave springs are placed between the channel box specimen and the supports to keep the channel box centered around the support pieces. The wave springs have minimal stiffness to allow the channel box to bow without applying any significant load, or stress on the channel box. Radial holes at the tops and bottoms of the tube specimens allow them to be secured to the internal supports using fasteners. The fasteners pass through the tube specimens and slots in the slotted pins, which are welded to the internal supports. This arrangement allows the tube specimens to bend and translate axially while maintaining their orientation inside the experiment.

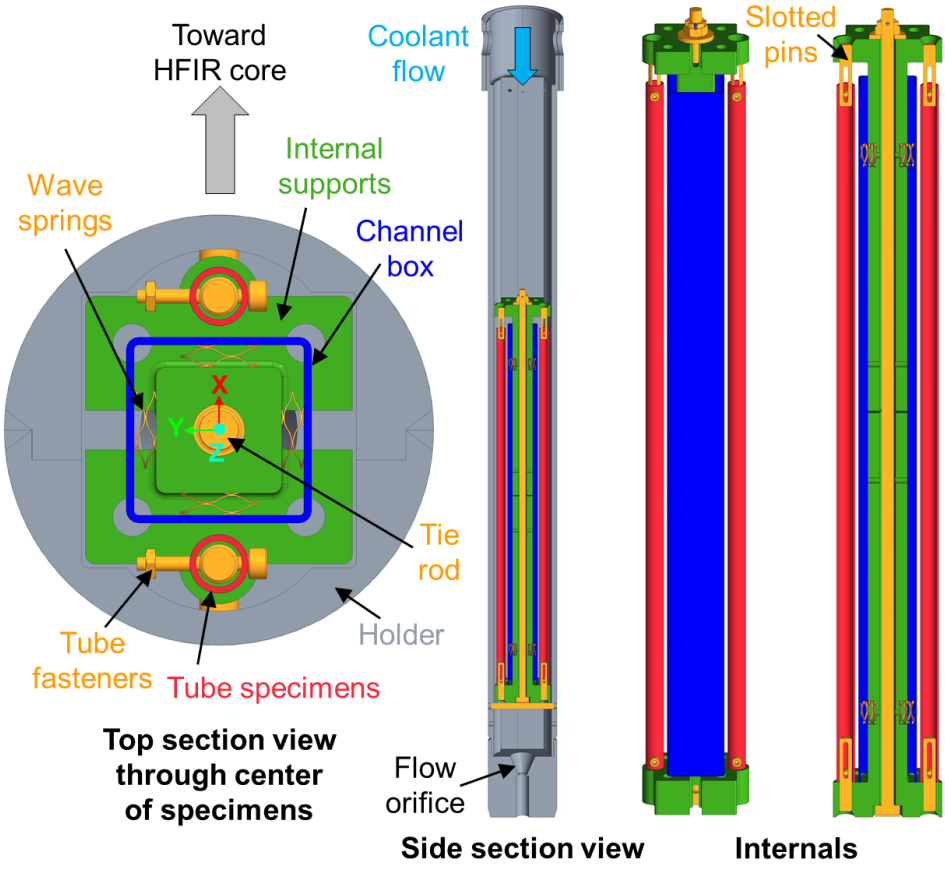

Figure 3. Design of the channel box experiment.

3. COMPUTATIONAL METHODS

3.1 Neutronics Analysis

Neutronics analyses were performed to determine the spatial variation in dose rate within the channel box specimen to provide input to the subsequent structural analyses. Analyses were performed using the MCNP5 software code package [30]. The MCNP calculations are based on existing fixed neutron source models of HFIR at beginning and end of cycle (BOC and EOC) with cycle 400 experimental loading [29]. Modifications were made to include the new experimental assembly inside VXF position 19, centered about the HFIR core midplane. The dose rates in the specimen were determined by tallying the neutron flux over a Cartesian mesh that was superimposed over the experiment and applying a weighting multiplier as follows [31]:

$$\dot{d} = \frac{0.8}{2E_d}\int_0^\infty \varphi(E)\sigma_d(E)dE \ . \tag{3}$$

where $\dot{d}$ is the dose rate, E_d is the average lattice displacement energy for SiC, $\varphi(E)$ is the energy-dependent neutron flux, and $\sigma_d(E)$ is the energy-dependent displacement damage cross section for SiC. The factor of 0.8 is an equivalent displacement efficiency [32]. The lattice displacement energy for SiC is taken to be 30 eV, which is the average of 40 eV for silicon and 20 eV for carbon [33]. The integral quantity is assessed from the MCNP tally of neutron flux weighted by the displacement damage cross section from the standard MCNP cross section libraries. In the absence of variance reduction techniques, statistical noise

is minimized by running 4×10^{10} particle histories for each calculation, yielding uncertainties well within 2% across the entire calculation mesh.

3.2 Structural Analysis

A three-dimensional (3D) structural FEA was performed using the ANSYS software package to estimate the bowing in the channel box during irradiation. The experiment was modeled using a mesh size of 0.5 mm for the X and Y directions and a 2 mm mesh size for the Z direction (see Figure 4). The origin is at the centroid of the channel box specimen. Figure 4 also shows how the channel box was constrained in the structural analysis. Symmetry was assumed along the XZ plane so that the displacement in the Y direction (U_Y) was constrained along this plane. Along the XY plane, displacement in the Z direction (U_Z) was constrained. Finally, the displacement in the X direction (U_X) was set equal to zero at a single point in the corner of the XY plane to prevent rigid body motion.

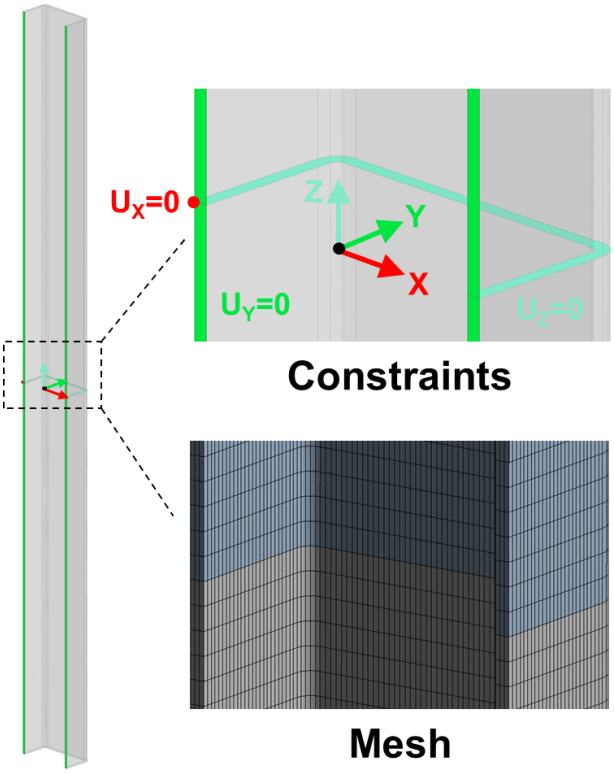

Figure 4. Structural model with displacement constraints and finite element mesh.

ANSYS has a built-in swelling model that requires the user to specify a spatially dependent neutron fluence and an equation to convert from fluence to linear swelling. For this work, the dose rates determined in the neutronics analysis (see previous section) were multiplied by the simulated irradiation time to give the total dose. Dose was converted to volumetric swelling using literature data from previous HFIR irradiation experiments performed at the same coolant temperatures [34]. The volumetric swelling was divided by a factor of 3 to convert to linear swelling (assumed isotropic swelling). The swelling vs. dose data obtained from the literature were fit to a power law to establish the dose-to-swelling model. The average specimen dose expected from one to two cycles of irradiation in a large VXF position in HFIR is expected be ~0.025 to 0.05 dpa (see Section 5.1). This dose range is between two of the experimental data points obtained from the literature, providing increased confidence in the validity of the dose-to-swelling model. Instead of inputting a representative neutron fluence profile into ANSYS, the linear swelling profile was imported

into ANSYS as a neutron fluence, and the fluence-to-swelling conversion was artificially set to unity. The structural analysis assumes only elastic deformation using an elastic modulus of 236 GPa. Previously reported values for nuclear-grade SiC/SiC composites fabricated using chemical vapor infiltration were in the range of 200–280 GPa [1]. The calculation assumed a constant temperature of 60°C. The effects of creep and pseudo-ductility due to microcracking were ignored. Creep was previously shown to have little impact on radiation-induced bowing [26], and the stresses are calculated to be well below typical proportional limit stresses for SiC/SiC composites (see Section 5.2). Simulations were performed for one and two HFIR irradiation cycles, each assumed to have a duration of 25 days.

4. EXPERIMENTAL METHODS

4.1 Specimen Fabrication

The SiC/SiC composite channel box was fabricated by GA. The channel box uses Hi-Nicalon Type-S SiC fibers with a nominally 150 nm thick pyrolytic carbon interphase surrounded by a SiC matrix formed by chemical vapor infiltration and a thin outer layer formed using chemical vapor deposition. The fiber architecture used two plies with a ±71° braiding angle. The nominal fiber volume fraction was 30–40%. The average macroscopic density was determined to be 2.5 g/cm^3. More details regarding GA's fabrication process can be found in a previous publication [10]. Figure 5 shows a picture of the channel box, 2D radiographs, and a 3D reconstruction of a section of a similar channel box obtained using x-ray computed tomography.

Figure 5. (a) Picture of the channel box, (b) two-dimensional radiographs, and (c) a three-dimensional reconstruction of a section of a similar channel box obtained using x-ray computed tomography.

4.2 Specimen Engraving

Laser engraving was performed to provide marks for determining local displacements after irradiation. Figure 6 shows pictures of the specimen after engraving, including a processed image of a single mark. Each face of the channel box was engraved with three rows of "X" marks separated by ~25 mm. Lines were engraved in the horizontal and vertical directions between marks and each mark was surrounded by an engraved circle. These features will help locate the fine markings on the rough surface of the channel box, especially after irradiation, when the measurement procedure may be more challenging owing to

radiological concerns. The engraving was performed using an ACSYS PIRANHA I FL20S laser marking system to achieve a line width of approximately 30 µm. Such a fine line width is necessary to accurately locate the center of each mark to determine post-irradiation displacements.

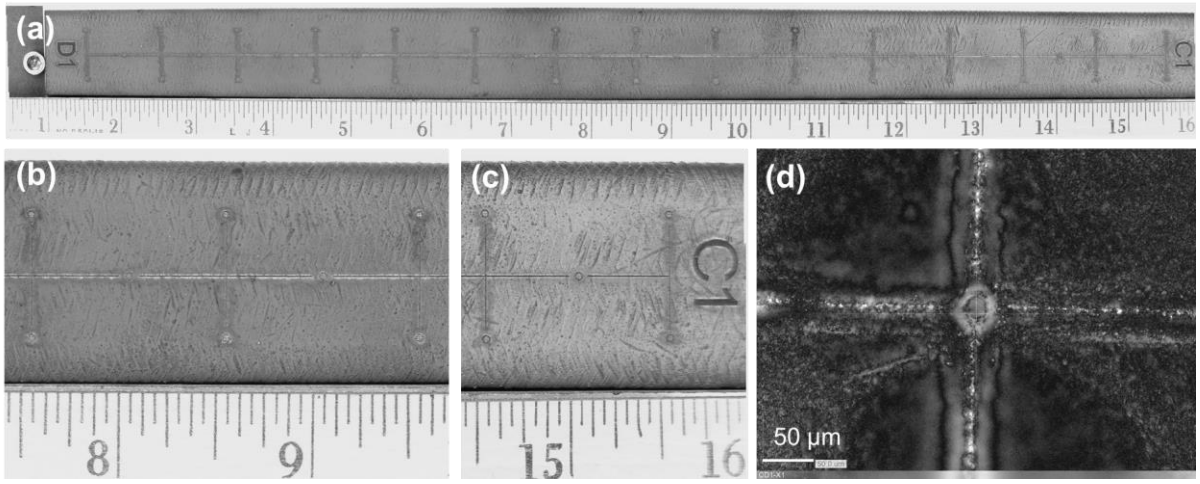

Figure 6. Photograph (a) of the engraved channel box specimen; (b, c) closer views of the engraved markers and (d) a processed image of a single marker.

4.3 Specimen Characterization

Specimens were first dimensionally inspected using micrometers and a height gauge for the length. Figure 7 summarizes the dimensional measurements. Three length measurements were made on each of the four faces of the channel box for a total of 12 measurements. These dimensions are denoted L_{ia}, L_{ib}, and L_{ic}, where "i" is the engraved index following the letter "C" or "D." The width (W_j) and depth (D_j) were measured at five equally spaced axial locations (j) along the length of the channel box. Wall thicknesses were measured on all four faces at both the top and bottom of the channel box and are denoted T_{Ci} and T_{Di}, respectively. Mass was measured to estimate the specimen density from the volume that was estimated using the volume displacement method.

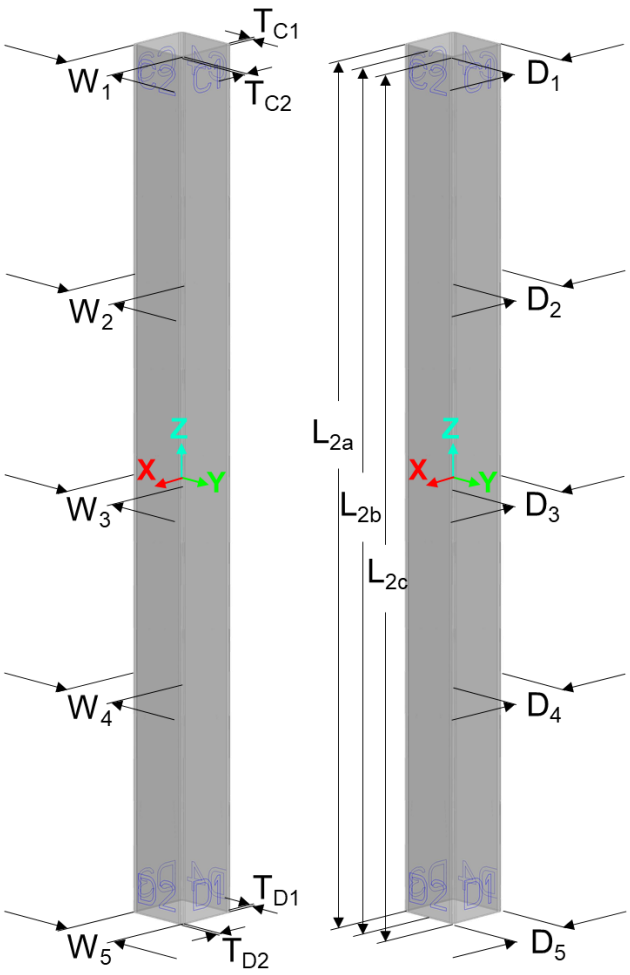

Figure 7. Labeling for dimensional inspection.

A custom profilometry system (Figure 8) was developed to more accurately characterize the channel box profile before and after irradiation. The system uses a Keyence LS-9030MR optical micrometer and a remotely-controlled, three-dimensional stage. The channel box was placed on its side on top of a polished and precisely machined stainless steel block. The optical profilometer was fixed to the stage adjacent to the specimen. The profilometer used edge detection to identify the top surface of the specimen and tracked the variation in the profile of this surface as the stage translated along the specimen's length. All profilometry data were post-processed using coordinate transformations so that the first and last points—corresponding to the top and bottom of the specimen, respectively—were coplanar, even if the specimen or the stage was not perfectly flat.

The profilometry stage also includes a mount for a digital microscope (Dino-Lite AF4115ZT for low magnification and Dino-Lite AM73515MT8A for high magnification) that looks down on the top of the specimen. The combination of the microscope (magnification >900X) and the stage allowed for precise determination of the distance between the engraved markers. The microscope was used to identify the center of each marker, and the X, Y, and Z coordinates from the stage were recorded for each marker. Figure 8a is labelled with face i=2 facing up, which orients the surface normal to the X direction. Image analysis can be performed to more precisely identify the center of the marker relative to the center of the image. The displacement measurements are expected to be accurate to within <10 μm, which is limited by the image

analysis rather than the accuracy of the stage (±1 µm). A ±10 µm displacement resolution corresponds to a linear strain resolution of ±0.01%.

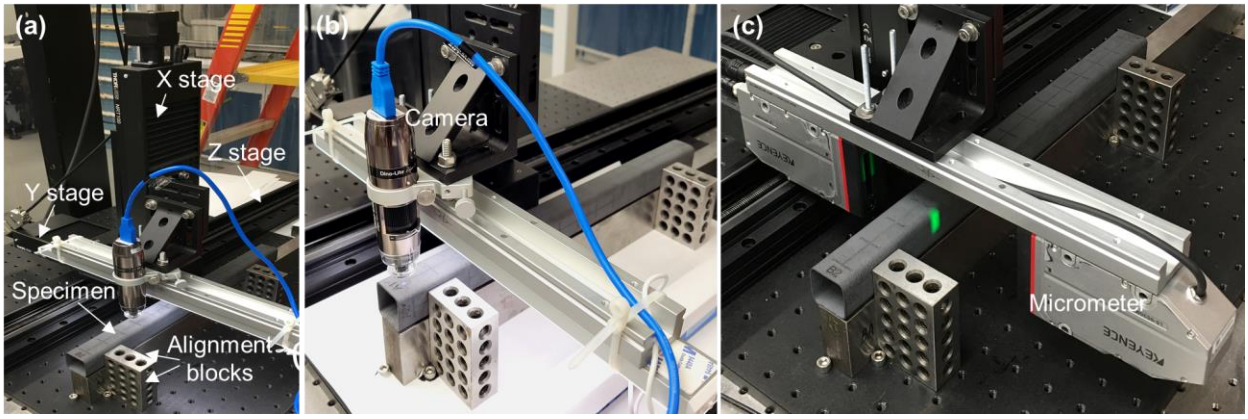

Figure 8. Pictures showing the translation stage that is used for both (a,b) local strain measurements with a digital microscope and (c) bowing measurements with an optical profilometer.

5. RESULTS

5.1 Neutronics Analysis

The spatially dependent dose rates in the channel box specimen are summarized in Figure 9. Because of the stochastic nature of the Monte Carlo calculations, the uncertainties in the calculated dose rates create artifacts that prevent a smooth spatial distribution even when 4×10^{10} source particles are used. These artifacts manifest as non-physical stresses in the structural analyses. To prevent these artifacts, the dose rate distributions were fit to an equation with the following form:

$$\dot{d}(\mathrm{X},\mathrm{Z}) = \dot{d}_{max}\, exp\left[\frac{\mathrm{X}-max\{\mathrm{X}\}}{\gamma_X}\right] exp\left[-\left(\frac{\mathrm{Z}}{\gamma_Z}\right)^2\right], \quad (4)$$

where $\dot{d}_{max}$ is the maximum simulated dose rate, γ_X determines the reduction in $\dot{d}$ with decreasing X, $max\{\mathrm{X}\} = 15$ mm is the maximum simulated value of X, and γ_Z determines the spatial profile of $\dot{d}$ with respect to Z. Because of symmetry, the spatial dependence of $\dot{d}$ on Y is not significant. Figure 9a and Figure 9b show BOC and EOC dose rates, respectively, vs. Z showing simulated data (solid lines) and fits (dashed lines). The fit parameters are summarized in Table 1, including the goodness-of-fit parameters R^2, which show that the data are well-represented by the fits. Figure 9c shows 3D dose rates at BOC (EOC profiles look similar) at Y=0 vs. X and Z. Figure 9d shows the dose rates and the spatial distributions of volumetric swelling in SiC at Y=0, Z=0 vs. X determined using the fit after one and two HFIR cycles. The Y location for Figure 9d was arbitrarily chosen because there is no significant variation in the calculated dose rate with respect to Y. The calculations predict a ~35% reduction in dose rate from the front face (facing toward the core) to the back face (facing away from the core) of the 30 mm square channel box specimen. This dose rate variation is similar to the 25–29% variation in fast neutron flux across approximately a dozen fresh channels in typical BWRs [23]. The magnitudes of the calculated dose rates are on the order of 10^{-5} dpa/hr, which are about an order of magnitude lower than those in a typical BWR. As shown in Figure 9d, the difference in volumetric swelling across the channel box increases significantly between cycles 1 and 2.

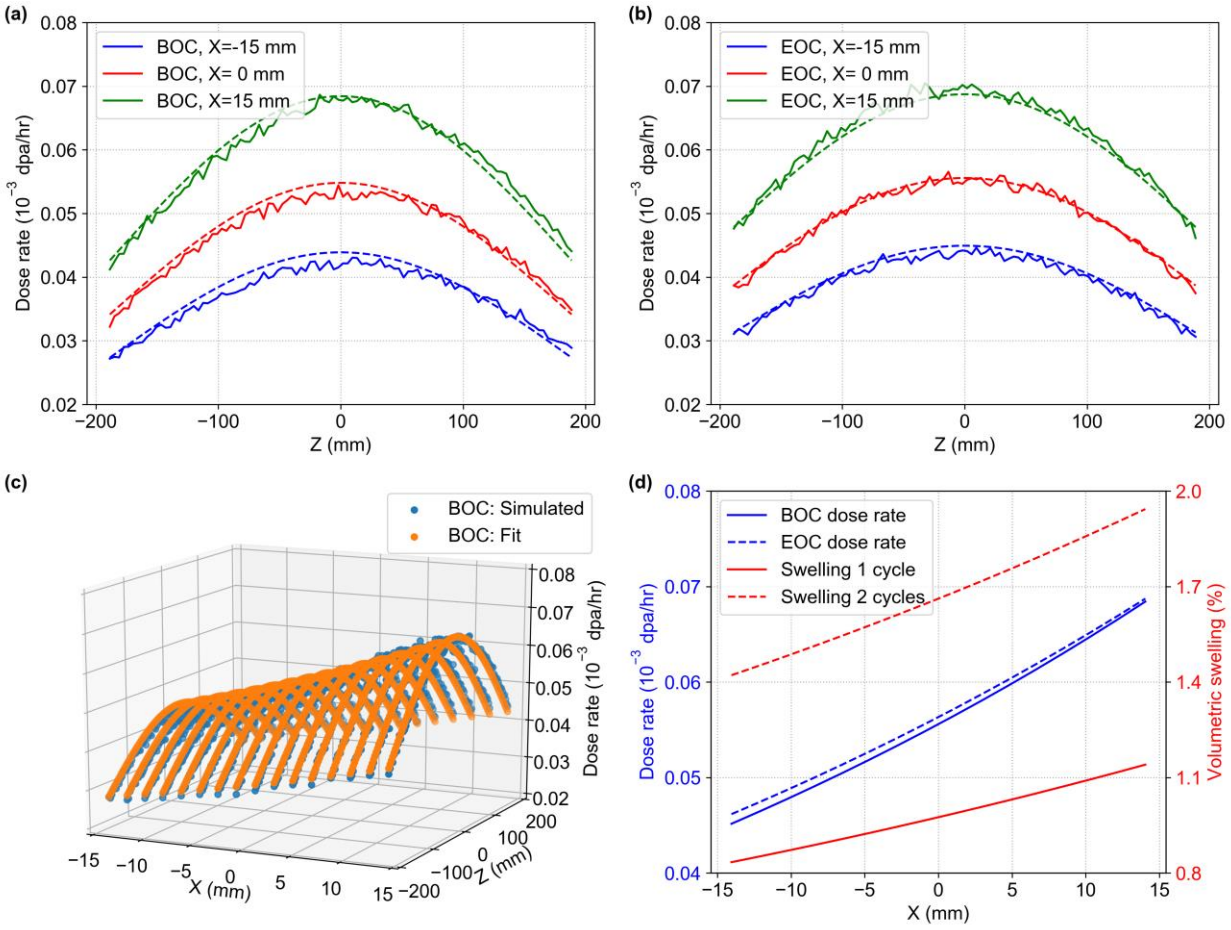

Figure 9. (a, b) BOC and EOC dose rates, respectively, at Y=0 and various X vs. Z showing simulated data (solid lines) and fits (dashed lines); (c) 3D BOC dose rates at Y=0 vs. X and Z showing simulated data and fits; (d) dose rate and volumetric swelling at Y=0, Z=0 vs. X determined using the fit after one and two HFIR cycles. The center of the HFIR core is in the positive X direction.

Table 1. Fitting parameters for the simulated dose rate distributions.

Time	$\dot{d}_{max}$ (dpa/hour)	γ_X (mm)	γ_Z (mm)	R^2
BOC	6.84×10^{-5}	67.6	274	0.984
EOC	6.87×10^{-5}	70.4	313	0.990

5.2 Structural Analysis

The 3D spatial distributions of volumetric swelling were input to structural finite element simulations. Figure 10 shows contour plots of the predicted lateral displacement U_X (in meters), as well as the normal stresses σ_X, σ_Y, and σ_Z (in Pa), after two cycles of irradiation. The visual deformations are artificially magnified by a factor of 10 in the displacement plot and a factor of 50 in the stress plots, and the undeformed structure is also shown as a wire frame. The stress distributions after one cycle are similar except with lower magnitudes. All stresses are relatively low with magnitudes of less than 13 MPa. In the Y direction (Figure

10b), the stresses transition from tension to compression through the thickness of the X-normal faces and are essentially neutral on the Y-normal faces. Similarly, the normal X stresses are neutral on the X-normal surfaces but transition from tension to compression moving in the X direction along the Y-normal surfaces. The Z-normal stresses become more compressive moving in the positive X direction along the X-normal faces. On the Y-normal faces, the Z-normal stresses have maximum tension in the center of the faces (X=0) and decrease moving in the positive and negative X direction.

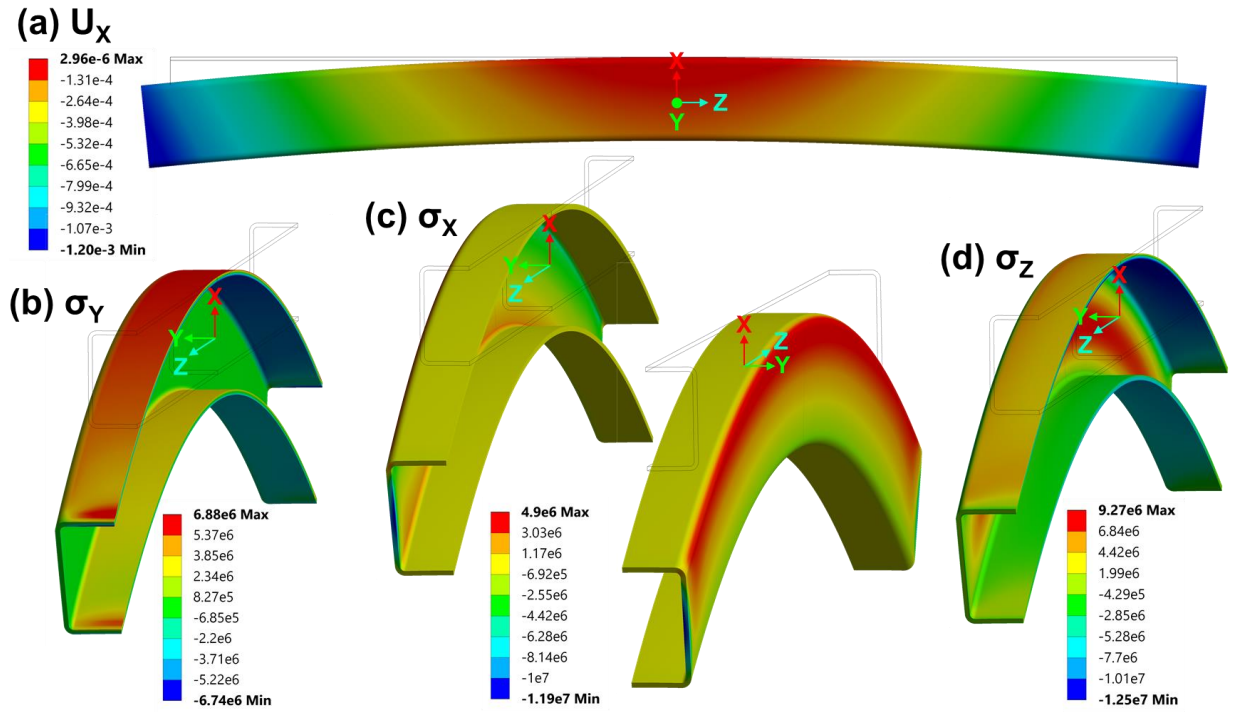

Figure 10. Simulated channel box bowing after two HFIR cycles showing (a) lateral displacement U_X (in m), with visual deformations artificially scaled by a factor of 10, and (b, c, d) normal stresses (in Pa) with visual deformations artificially scaled by a factor of 50.

Figure 11 shows U_X as a function of Z, with the number of cycles as a parameter. Results were obtained using FEA and analytical Eqs. (1) and (2). The analytical equations used swelling data from Figure 9d evaluated at Z=0 mm to determine $\left(\frac{dV}{V}\right)_{diff}$. The fact that the FEA results are essentially identical to the analytical results shows that the bowing is primarily dictated by differential swelling at Z=0 mm and that the axial variation in dose rate does not have a significant effect. The lateral bowing shown in Figure 11 is defined as the maximum lateral displacement for all nodes at a given Z position relative to the maximum lateral displacement at Z=0 mm. In this way, the lateral bowing compensates for the swelling of the channel box in the X direction. The lateral displacements in Figure 10 include the effects of bowing and swelling in the X direction. This explains why the maximum absolute value of U_X in Figure 10 (1.2 mm) is slightly larger than that in Figure 11 (1.02 mm) after two cycles of irradiation.

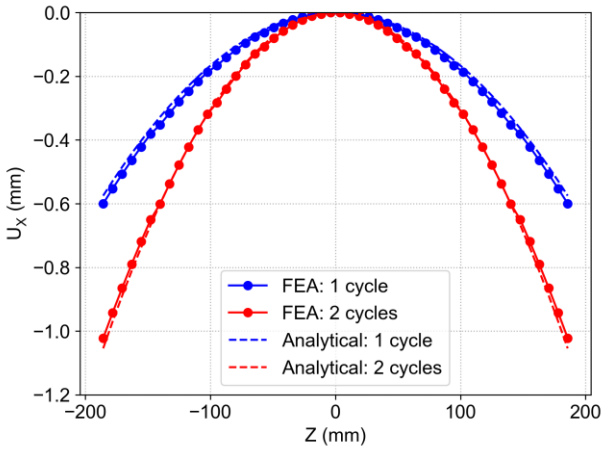

Figure 11. Lateral bowing profiles determined using FEA and analytical equations after 1 and 2 HFIR cycles.

5.3 Pre-Irradiation Characterization

5.3.1 Dimensional Inspection

The channel box was first dimensionally inspected to provide a reference to which post-irradiation measurements can be compared. Table 2 summarizes the dimensional inspection using the notation in Figure 7.

Table 2. Summary of pre-irradiation dimensional inspections.

Mass (g)	100.2936				
	i = 1	i = 2	i = 3	i = 4	
L_{ia} (mm)	382.226	382.122	382.484	382.920	
L_{ib} (mm)	382.480	382.105	382.386	382.698	
L_{ic} (mm)	382.686	382.089	382.341	382.680	
T_{Ci} (mm)	1.188	1.229	1.152	1.288	
T_{Di} (mm)	1.327	1.028	1.380	1.191	
	j = 1	j = 2	j = 3	j = 4	j = 5
W_j (mm)	29.614	29.418	29.705	29.606	29.295
D_j (mm)	29.391	29.846	29.169	29.123	30.053

5.3.2 Profilometry

Profilometry measurements were performed to compare the detailed specimen profiles before and after irradiation. Before the channel box specimen was measured, two calibration measurements were performed. First, a nominally straight stainless steel bar was scanned to ensure that the system did not introduce significant artifacts into the measurements. After scanning the bar in one direction, the bar was reversed and rescanned. The maximum profile variation of the stainless steel bar was measured to be 3–4 µm using a dial indicator. Next, an aluminum square (31.75 mm width) channel specimen was procured and bent around a mandrel to introduce a nominal bow of 0.76 mm. Figure 12 shows the profilometry measurements for these scans. Figure 12a shows a maximum profile deviation in the range of ~28 µm. Because the forward and reversed scans show similar profiles, the 28 µm profile variations are likely

caused by slight bowing of the track along which the profilometer travels. However, the 28 µm profile variation is much less than the expected radiation-induced bowing (see Figure 11). Furthermore, this variation would be present in both pre-irradiation and post-irradiation measurements. Therefore, the effects of the variation in the profilometer track can be compensated by subtracting the pre-irradiation surface profile from the post-irradiation profile.

Figure 12b shows that in the planes of the intentional bow ("1L to 1R" and "3L to 3R"), the measured bow is consistent with the nominal value of 0.76 mm. Furthermore, the system clearly shows that the surface labeled "3L to 3R" has more localized deformation near the center of the specimen, likely because the mandrel contacted the specimen on this face during the bending operations. The measurements in the "2L to 2R" and "4L to 4R" planes do not show significant bowing, as expected. The large profile variations in the "2L to 2R" plane are caused by tape that was placed on this surface to identify the specimen.

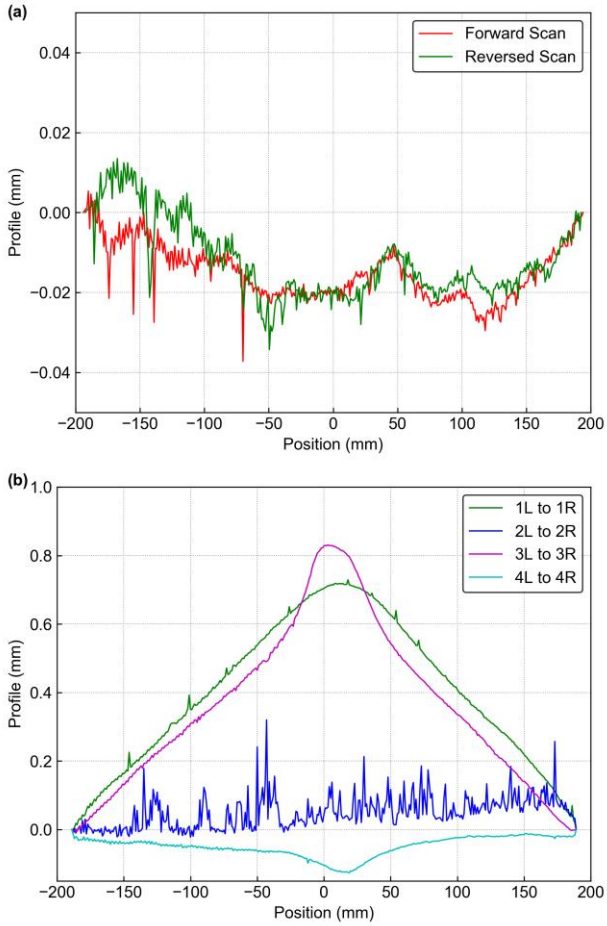

Figure 12. Profilometry calibration scans of (a) a straight stainless steel bar and (b) a dummy aluminum square channel with a nominally 0.76 mm bow introduced by bending around a mandrel.

Figure 13 shows the profilometry measurements for the channel box specimen. The position data (Z, horizontal axis) are reversed in these plots so that following the profiles from left to right in Figure 13 is equivalent to following the specimen profiles from top to bottom (i.e., from engraved markers "Ci" to "Di"). The roughness of the composite specimen's surfaces is evident in the specimen profiles. Therefore, a third-order Savitzky–Golay filter was used with a 15-point window (15 mm in the Z direction) to filter

the effects of the specimen's surface roughness. Figure 13a shows the measured data (solid lines) and the filtered data (dashed lines). Because the filtered data are difficult to see, Figure 13b shows only the filtered data. The parallel C1 D1 (red lines) and C3 D3 (blue lines) faces generally show a positive bow with a maximum value of 0.67 mm on the C3 D3 face. Both faces show a sharp decrease in the profile near Z=105 mm. This decrease is consistent with the specimen width decreasing from W_1 to W_2 and then increasing from W_2 to W_3 (see Table 2). The differences in the C1 D1 and C3 D3 profiles for Z<90 mm must be a result of features that are present on one face and not on the other. Similar differences can be observed between the C2 D2 and C4 D4 faces, although some common features can be observed that could be attributed to bending or bowing. Examples include the decreases observed from Z = 160 to 189 mm and the increase and plateau observed from Z=-70 to 46 mm.

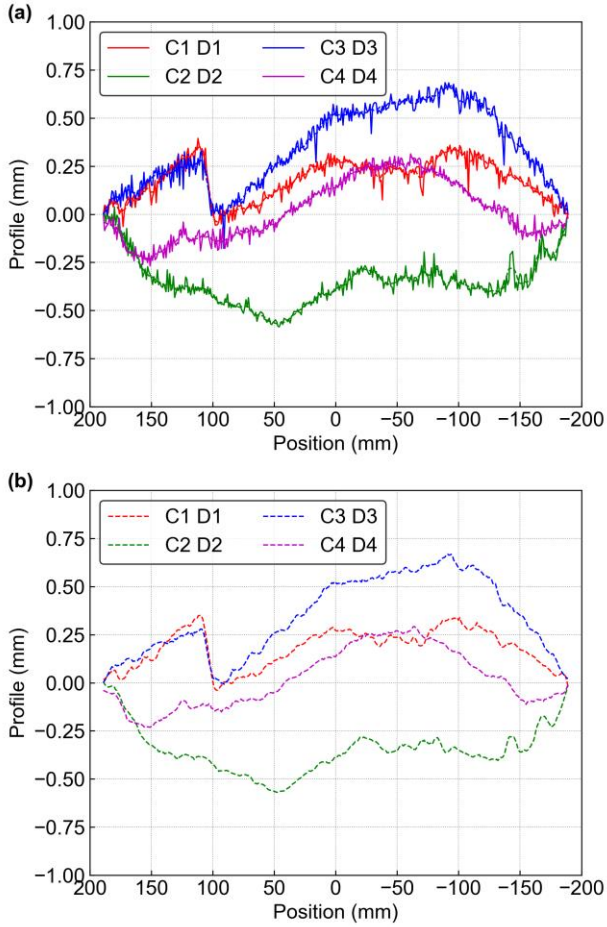

Figure 13. Profile measurements for the channel box specimen showing (a) measured data (solid lines) and filtered data (dashed lines), and (b) only the filtered data.

5.3.3 Marker Spacing for Local Strain Mapping

Figure 14 shows the locations that were measured for each marker before irradiation. The individual marker locations are summarized in the Appendix. For reference, Figure 14a shows the configuration for the various specimen faces. The dashed black lines in Figure 14b outline the outer surface of each face. The single red marker on face C3 D3 is questionable because one coordinate is thought to have been transposed during the recording process. The corrected coordinate is shown; however, because it is not certain whether a transposing error occurred, this marker has been flagged. Additional image analysis is currently under way to increase the precision of the marker spacing measurements by determining the

deviation of the centroid of each marker relative to the center of each image (see Figure 6d for an example).

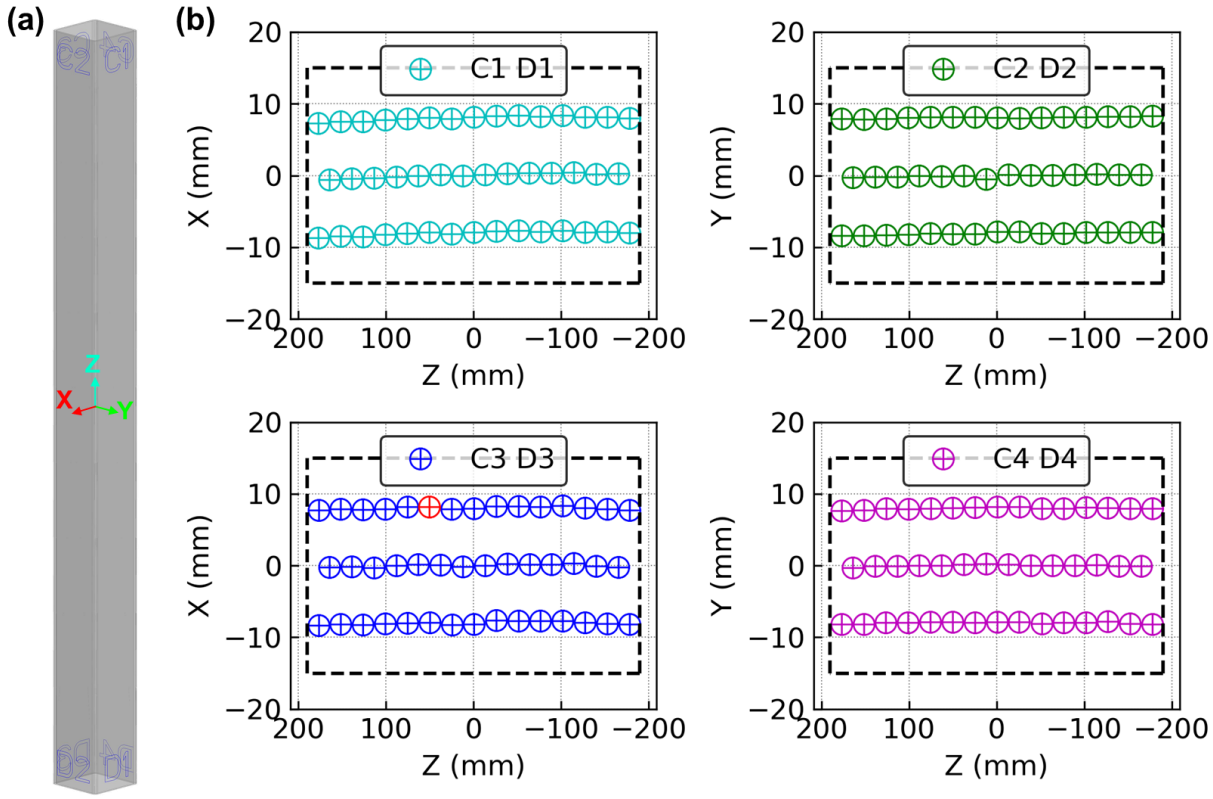

Figure 14. Measured engraved marker locations showing (a) the configuration for the various specimen faces and (b) the measured marker locations. The outer surfaces of each face are shown as dashed black lines. The single red marker on face C3 D3 is questionable because one coordinate is thought to have been transposed during the recording process. Because this is not certain, this marker has been flagged.

5.4 Experiment Assembly

The first step in the experiment assembly involved welding the outer aluminum holder. Figure 15 shows pictures of the holder components before (a, b, c) and after (d, e, f) assembly. The two halves of the holder body were welded in two places at three axial heights. Three of the weld locations on one side of the holder that were later filled can be seen in Figure 15c. The bottom orifice was welded to the bottom of the holder body halves. A top ring was also welded to provide additional structural support to prevent the holder from splitting at its top. Finally, a rod was inserted through both holder halves and welded in place to provide a support upon which the internal components rested. The orifice and welded rod are visible in Figure 15e.

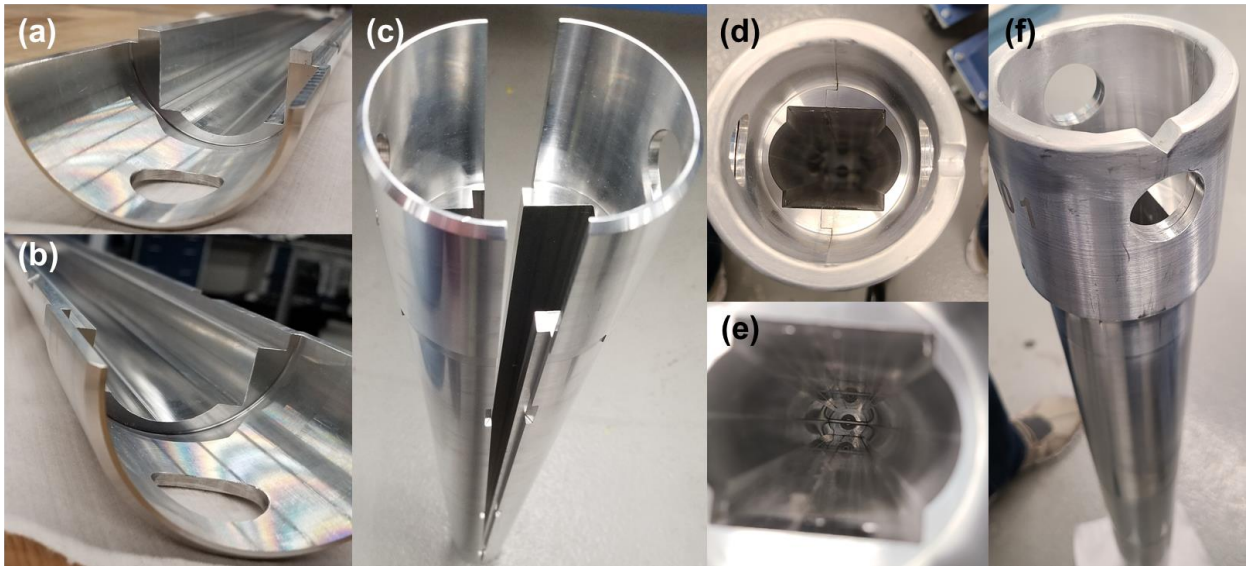

Figure 15. Photographs of the holder assembly.

Next, the internal components were assembled. Figure 16 shows the parts layout and Figure 17 shows the assembly process. The slotted pins were welded to the bases of the internal supports and wave springs were inserted into the matching holes in the sides of the internal supports. The channel box specimen was placed around one of the two internal supports as the wave springs were compressed. The tube specimens were placed over each of the slotted pins that were welded to the same internal support and were then secured using fasteners. This assembly was then lowered onto the second internal support while aligning the tube specimens and the channel box. Fasteners were secured to the opposite ends of the tube specimens, and the tie rod was inserted through both internal supports and secured at the top using a lock nut and cotter pin. The entire internal assembly was then lowered into the holder until it came to rest on the welded rod.

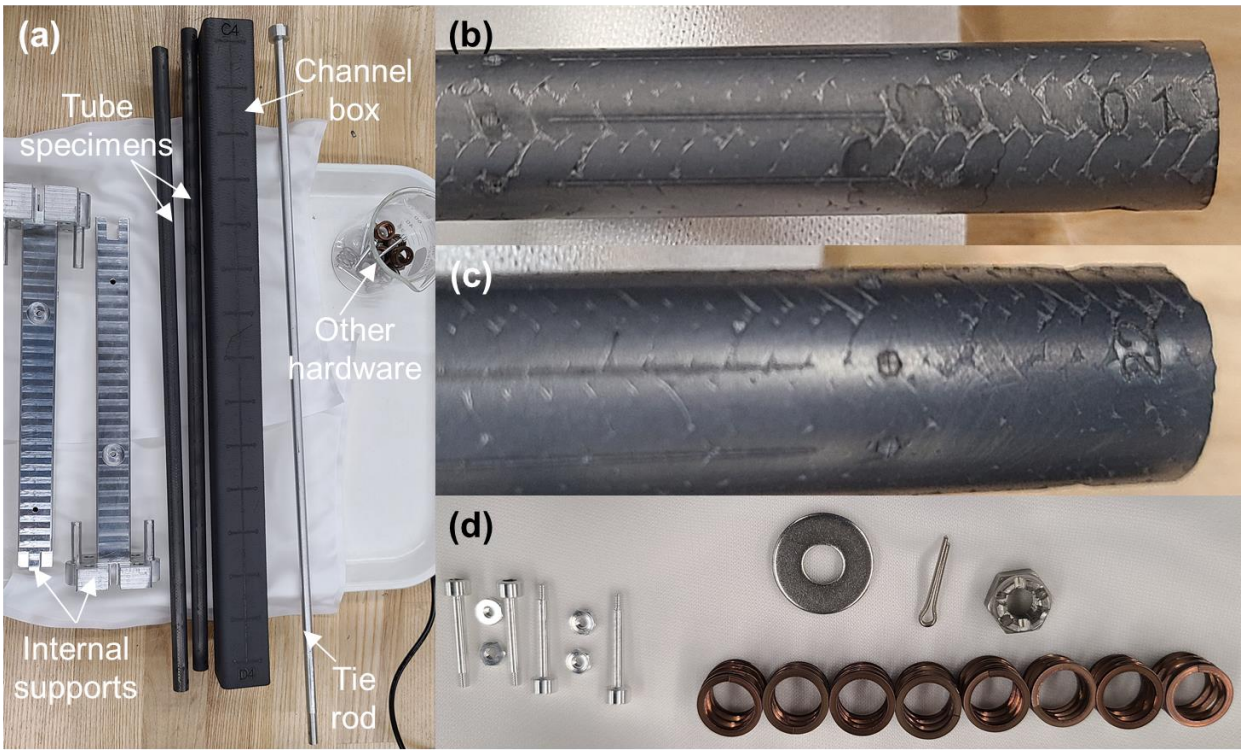

Figure 16. Photographs of the internal experiment components.

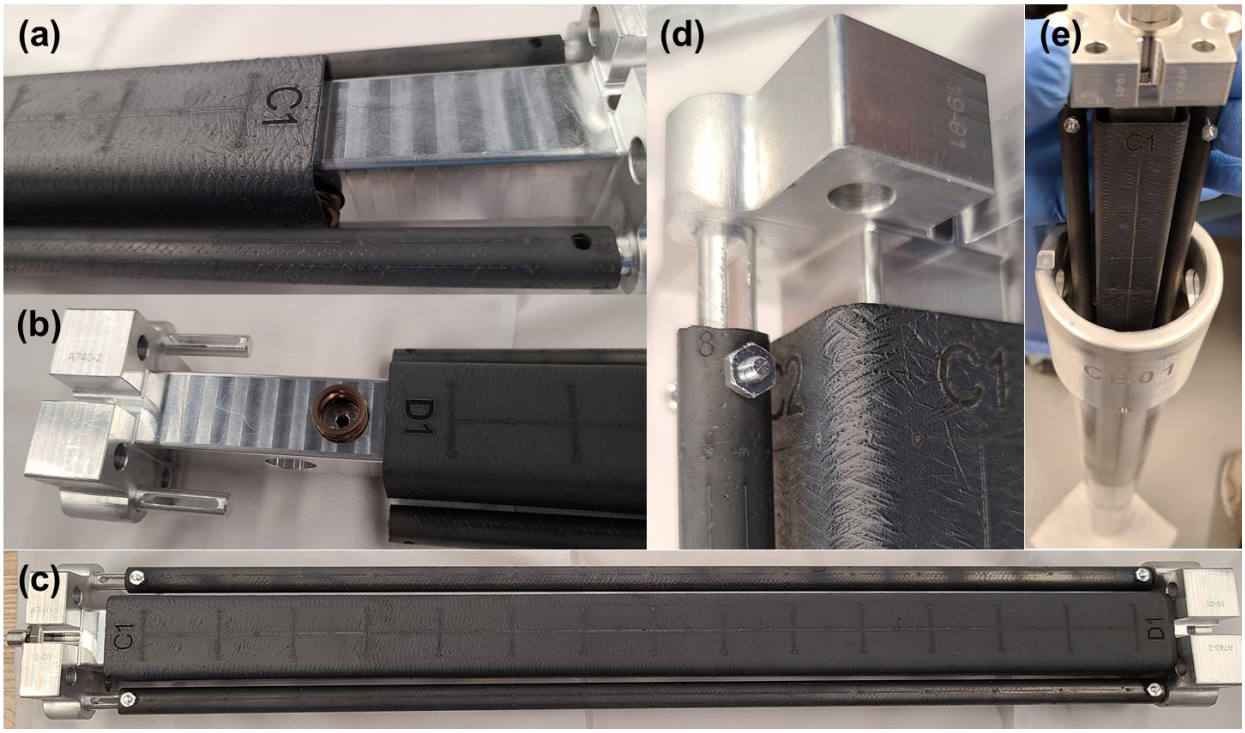

Figure 17. Photographs of the internal assembly.

The experiment assembly was properly packaged and transported to HFIR along with a fabrication package that includes all material certification, dimensional inspection, weld reports, safety calculations, and signed procedures. The package was reviewed and accepted by all irradiation engineers, quality assurance personnel, and HFIR safety staff. Some of the experiment approval forms are included in the Appendix in this report. The experiment is scheduled for insertion during HFIR cycle 492, which is currently scheduled to run from May 18, 2021 to June 11, 2021.

6. SUMMARY AND CONCLUSIONS

This report summarizes the motivation, design, pre-irradiation characterization, and successful assembly of a HFIR irradiation experiment with the goal of validating thermomechanical models for radiation-induced bowing of SiC/SiC composite components for LWR applications. Calculations have predicted significant lateral bowing of SiC/SiC components during exposure to either a differential radial fast neutron flux gradient or a significant radial temperature gradient during irradiation. This experiment is targeting the former scenario, as the HFIR's reflector positions provide a significant radial fast neutron flux gradient, similar to what might be expected for a BWR channel box positioned at the periphery of the core. The HFIR experiment will irradiate a miniature SiC/SiC channel box and two SiC/SiC specimens with a prototypic PWR diameter for one to two cycles (each ~25 days). The specimens will be directly cooled by the reactor coolant, which remains at a temperature of approximately 50−60°C. Neutronics analyses predict a ~35% reduction in dose rate from the front face (facing toward the core) to the back face (facing away from the core) of the 30 mm square channel box specimen. This results in calculated differential radiation-induced swelling of 0.3 vol % and 0.55 vol % after one and two irradiation cycles, respectively. The structural analyses predict bowing of 0.60 mm and 1.02 mm at the end of one and two cycles of irradiation, respectively. Calculated normal stresses are relatively, on the order of megapascals and less than 13 MPa for all evaluated cases.

In addition to typical dimensional inspections (length, width, depth, and wall thickness), the channel box specimen was engraved with fine markers for mapping local strains and profiled using an optical micrometer to accurately characterize any bowing that may be present before irradiation. Those measurements will be repeated post-irradiation to quantify radiation-induced bowing. The pre-irradiation bowing was measured to be as large as 0.67 mm on one face and as small as 0.25 mm on another, indicating that the expected radiation-induced bowing (0.6 mm or greater) can be measured. The spacing between engraved markers was measured using a 3D stage and a digital microscope. Additional analysis is being performed to provide a fine adjustment to the marker spacing by determining the distance from the center of each image to the centroid of the engraved markers. It is expected that the spacing can be quantified to within less than 10 μm, which is equivalent to ±0.01% linear strain (±0.03% volumetric swelling). The experiment was successfully assembled and is scheduled for insertion during HFIR cycle 492, which is currently scheduled to run from May 25, 2021 to June 18, 2021.

7. REFERENCES

1. Katoh, Y., et al., *Continuous SiC fiber, CVI SiC matrix composites for nuclear applications: Properties and irradiation effects.* Journal of Nuclear Materials, 2014. **448**(1–3): p. 448–476.
2. Koyanagi, T., et al., *Effects of neutron irradiation on mechanical properties of silicon carbide composites fabricated by nano-infiltration and transient eutectic-phase process.* Journal of Nuclear Materials, 2014. **448**(1–3): p. 478–486.
3. Ishikawa, T., et al., *A Tough, Thermally Conductive Silicon Carbide Composite with High Strength up to 1600°C in Air.* Science, 1998. **282**(5392): p. 1295.
4. Katoh, Y., et al., *Dimensional stability and anisotropy of SiC and SiC-based composites in transition swelling regime.* Journal of Nuclear Materials, 2018. **499**: p. 471-479.

5. Katoh, Y., et al., *Stability of SiC and its composites at high neutron fluence.* Journal of Nuclear Materials, 2011. **417**(1–3): p. 400–405.
6. George, N.M., et al., *Neutronic analysis of candidate accident-tolerant cladding concepts in pressurized water reactors.* Annals of Nuclear Energy, 2015. **75**: p. 703-712.
7. Terrani, K.A., et al., *Silicon Carbide Oxidation in Steam up to 2 MPa.* Journal of the American Ceramic Society, 2014. **97**(8): p. 2331–2352.
8. Pint, B.A., et al., *High temperature oxidation of fuel cladding candidate materials in steam–hydrogen environments.* Journal of Nuclear Materials, 2013. **440**(1): p. 420-427.
9. Deck, C.P., et al., *Fabrication of SiC–SiC composites for fuel cladding in advanced reactor designs.* Progress in Nuclear Energy, 2012. **57**: p. 38-45.
10. Deck, C.P., et al., *Characterization of SiC–SiC composites for accident tolerant fuel cladding.* Journal of Nuclear Materials, 2015. **466**: p. 667–681.
11. Zinkle, S.J., et al., *Accident tolerant fuels for LWRs: A perspective.* Journal of Nuclear Materials, 2014. **448**(1-3): p. 374–379.
12. Terrani, K.A., *Accident tolerant fuel cladding development: Promise, status, and challenges.* Journal of Nuclear Materials, 2018. **501**: p. 13-30.
13. Ott, L.J., K.R. Robb, and D. Wang, *Preliminary assessment of accident-tolerant fuels on LWR performance during normal operation and under DB and BDB accident conditions.* Journal of Nuclear Materials, 2014. **448**(1): p. 520-533.
14. Terrani, K.A., et al., *Hydrothermal corrosion of SiC in LWR coolant environments in the absence of irradiation.* Journal of Nuclear Materials, 2015. **465**: p. 488-498.
15. Kondo, S., et al., *Effect of irradiation damage on hydrothermal corrosion of SiC.* Journal of Nuclear Materials, 2015. **464**: p. 36-42.
16. Stempien, J.D., et al., *Characteristics of Composite Silicon Carbide Fuel Cladding after Irradiation under Simulated PWR Conditions.* Nuclear Technology, 2013. **183**(1): p. 13-29.
17. Ben-Belgacem, M., et al., *Thermo-mechanical analysis of LWR SiC/SiC composite cladding.* Journal of Nuclear Materials, 2014. **447**(1–3): p. 125–142.
18. Stone, J.G., et al., *Stress analysis and probabilistic assessment of multi-layer SiC-based accident tolerant nuclear fuel cladding.* Journal of Nuclear Materials, 2015. **466**: p. 682–697.
19. Petrie, C.M., et al., *Experimental design and analysis for irradiation of SiC/SiC composite tubes under a prototypic high heat flux.* Journal of Nuclear Materials, 2017. **491**: p. 94–104.
20. Singh, G., et al., *Evaluating the irradiation effects on the elastic properties of miniature monolithic SiC tubular specimens.* Journal of Nuclear Materials, 2018. **499**: p. 107-110.
21. Singh, G., K. Terrani, and Y. Katoh, *Thermo-mechanical assessment of full SiC/SiC composite cladding for LWR applications with sensitivity analysis.* Journal of Nuclear Materials, 2018. **499**: p. 126-143.
22. Singh, G., et al., *Elastic moduli reduction in SiC-SiC tubular specimen after high heat flux neutron irradiation measured by resonant ultrasound spectroscopy.* Journal of Nuclear Materials, 2019. **523**: p. 391-401.
23. Yueh, K. and K.A. Terrani, *Silicon carbide composite for light water reactor fuel assembly applications.* Journal of Nuclear Materials, 2014. **448**(1–3): p. 380–388.
24. Garzarolli, F., et al., *BWR Fuel Channel Distortion*. 2011, Advanced Nuclear Technology International: Mölnlycke, Sweden.
25. Snead, L.L., et al., *Handbook of SiC properties for fuel performance modeling.* Journal of Nuclear Materials, 2007. **371**(1–3): p. 329–377.
26. Singh, G., et al., *Deformation analysis of SiC-SiC channel box for BWR applications.* Journal of Nuclear Materials, 2019. **513**: p. 71-85.
27. Singh, G., et al., *Parametric Evaluation of SiC/SiC Composite Cladding with UO2 Fuel for LWR Applications: Fuel Rod Interactions and Impact of Nonuniform Power Profile in Fuel Rod.* Journal of Nuclear Materials, 2018. **499**: p. 155-167.

28. Cheverton, R.D. and T.M. Sims, *HFIR Core Nuclear Design*. 1971, Oak Ridge National Laboratory: Oak Ridge, TN.
29. Xoubi, N. and R.T. Primm III, *Modeling of the High Flux Isotope Reactor Cycle 400*. 2005: Oak Ridge, TN.
30. X-5 Monte Carlo Team, *Monte Carlo Team, MCNP–A General Purpose Monte Carlo N-Particle Transport Code, Version 5*. 2003, Los Alamos National Laboratory.
31. Norgett, M.J., M.T. Robinson, and I.M. Torrens, *A proposed method of calculating displacement dose rates.* Nuclear Engineering and Design, 1975. **33**(1): p. 50-54.
32. Robinson, M.T. and I.M. Torrens, *Computer simulation of atomic-displacement cascades in solids in the binary-collision approximation.* Physical Review B, 1974. **9**(12): p. 5008-5024.
33. Zinkle, S.J. and C. Kinoshita, *Defect production in ceramics.* Journal of Nuclear Materials, 1997. **251**: p. 200–217.
34. Snead, L.L., et al., *Dimensional isotropy of 6H and 3C SiC under neutron irradiation.* Journal of Nuclear Materials, 2016. **471**: p. 92-96.

APPENDIX A. MEASURED LOCATIONS OF ENGRAVED MARKERS AND EXPERIMENT FABRICATION DOCUMENTATION

Face C1 D1			
Marker ID	**Z (mm)**	**X (mm)**	**Surface normal distance (mm)**
1	577.479	70.968	93.270
2	577.503	86.976	93.090
3	564.797	79.064	93.220
4	552.067	71.188	93.330
5	552.177	87.209	93.120
6	539.398	79.225	93.210
7	526.608	71.155	93.390
8	526.620	87.180	93.230
9	513.905	79.266	93.370
10	501.188	71.395	93.060
11	501.289	87.409	93.020
12	488.515	79.433	92.970
13	476.202	71.575	92.990
14	476.181	87.574	93.070
15	463.499	79.638	93.040
16	450.807	71.752	93.040
17	450.869	87.760	93.230
18	438.120	79.754	93.120
19	425.287	71.544	93.120
20	425.300	87.567	93.300
21	412.580	79.634	93.290
22	399.870	71.748	93.190
23	399.949	87.771	93.390
24	387.171	79.765	93.200
25	374.645	71.894	93.090
26	374.749	87.993	93.310
27	361.958	79.965	93.170
28	349.300	71.961	93.050
29	349.408	88.002	93.270
30	336.841	79.997	93.170
31	323.924	71.818	93.080
32	324.096	87.914	93.320
33	311.377	80.001	93.220
34	298.796	71.940	93.160
35	298.773	88.007	93.360
36	286.168	80.059	93.220
37	273.155	71.783	93.070
38	273.185	87.792	93.270
39	260.515	79.874	93.100
40	247.973	71.811	93.000
41	247.936	87.836	93.160
42	235.377	79.894	92.990
43	222.228	71.661	92.840
44	222.188	87.644	93.020

Face C2 D2			
Marker ID	**Z (mm)**	**Y (mm)**	**Surface normal distance (mm)**
1	578.454	70.810	93.980
2	578.583	87.042	93.505
3	565.708	78.889	93.819
4	552.930	70.794	94.078
5	553.141	87.021	93.656
6	540.415	78.991	93.918
7	527.492	70.901	94.108
8	527.667	87.071	93.696
9	514.893	78.945	93.898
10	502.125	70.953	94.137
11	502.340	87.197	93.676
12	489.607	79.092	93.858
13	476.890	71.072	94.117
14	476.898	87.320	93.756
15	464.297	79.047	93.985
16	451.380	71.023	94.177
17	451.583	87.277	93.826
18	438.917	79.162	93.945
19	426.214	71.029	94.107
20	426.336	87.308	93.706
21	413.108	78.693	93.885
22	400.932	71.329	93.967
23	400.822	87.245	93.696
24	388.127	79.286	93.665
25	375.466	71.299	93.767
26	375.258	87.177	93.536
27	362.496	79.212	93.595
28	350.121	71.129	93.607
29	350.041	87.222	93.666
30	337.377	79.182	93.585
31	324.698	71.121	93.507
32	324.632	87.276	93.686
33	312.281	79.255	93.645
34	299.499	71.217	93.517
35	299.615	87.303	93.706
36	287.037	79.340	93.715
37	274.240	71.286	93.557
38	274.324	87.400	93.725
39	261.695	79.320	93.675
40	248.939	71.279	83.547
41	248.944	87.355	93.845
42	236.329	79.247	93.655
43	223.524	71.273	93.407
44	223.617	87.440	93.755

Marker locations for faces C1 D1 and C2 D2.

Face C3 D3			
Marker ID	**Z (mm)**	**X (mm)**	**Surface normal distance (mm)**
1	577.668	71.412	93.865
2	577.740	87.452	93.585
3	565.120	79.490	93.715
4	552.408	71.604	93.835
5	552.440	87.623	93.495
6	539.782	79.621	93.765
7	526.898	71.466	93.885
8	526.839	87.529	93.645
9	514.280	79.450	93.805
10	501.660	71.648	93.705
11	501.636	87.642	93.435
12	489.014	79.762	93.355
13	476.459	71.758	93.565
14	476.494	87.908	93.415
15	463.880	79.881	93.545
16	450.986	71.796	93.705
17	451.108	87.924	93.515
18	438.439	79.800	93.705
19	425.450	71.499	93.915
20	425.586	87.615	93.703
21	412.928	79.622	93.875
22	400.137	71.542	94.015
23	400.337	87.724	93.843
24	387.593	79.764	93.925
25	375.060	72.092	93.995
26	374.976	88.039	93.873
27	362.444	79.982	93.855
28	349.635	72.029	93.985
29	349.584	88.031	93.883
30	336.980	79.952	93.875
31	324.323	72.020	93.975
32	324.416	87.910	93.883
33	311.724	79.919	93.955
34	299.195	72.061	94.045
35	299.065	88.099	93.913
36	286.414	80.078	93.955
37	273.637	71.827	93.915
38	273.519	87.752	93.833
39	260.912	79.692	93.775
40	248.178	71.673	93.625
41	248.140	87.643	93.683
42	235.383	79.530	93.575
43	222.780	71.597	93.475
44	222.666	87.503	93.403

Face C4 D4			
Marker ID	**Z (mm)**	**Y (mm)**	**Surface normal distance (mm)**
1	577.245	70.091	92.560
2	577.068	85.885	92.250
3	564.368	77.957	92.477
4	551.823	70.123	92.630
5	551.664	85.978	92.330
6	539.161	78.165	92.547
7	526.589	70.362	92.620
8	526.424	86.209	92.270
9	513.559	78.208	92.430
10	501.035	70.304	92.570
11	500.785	86.169	92.250
12	488.296	78.275	92.400
13	475.764	70.408	92.670
14	475.514	86.248	92.210
15	462.993	78.247	92.470
16	450.418	70.412	92.720
17	450.246	86.279	92.330
18	437.720	78.456	92.480
19	425.117	70.363	92.690
20	424.985	86.373	92.310
21	412.419	78.501	92.440
22	399.613	70.421	92.600
23	399.653	86.423	92.250
24	386.968	78.448	92.400
25	374.272	70.394	92.500
26	374.239	86.442	92.140
27	361.467	78.244	92.270
28	348.755	70.142	92.570
29	348.753	86.213	92.180
30	336.149	78.239	92.340
31	323.489	70.300	92.670
32	323.549	86.234	92.270
33	310.991	78.285	92.590
34	298.317	70.355	92.850
35	298.262	86.349	92.460
36	285.739	78.339	92.770
37	273.079	70.449	93.090
38	273.066	86.331	92.670
39	260.324	78.196	93.020
40	247.556	70.166	93.300
41	247.534	86.257	92.930
42	234.899	78.209	93.100
43	222.063	70.080	93.320
44	222.122	86.192	92.980

Marker locations for faces C3 D3 and C4 D4.

Capsule Fabrication Request Sheet

Page 1 of 1
Date 3/3/2021

Target ID: CB01

Irradiation Conditions

Number cycles	2
First Cycle Goal	492
Assembly drawing	X3E020977A741 Rev.1

Approvals

	Request	Build
Performed by:	Annabelle Le Coq (Digitally signed by Annabelle Le Coq Date: 2021.03.03 11:46:55 -05'00')	David Bryant (Digitally signed by David Bryant Date: 2021.03.03 15:13:39 -05'00')
Checked by:	Christian M. Petrie (Digitally signed by Christian M. Petrie Date: 2021.03.03 13:25:56 -05'00')	Nicholas George Russell (Digitally signed by Nicholas George Russell Date: 2021.03.04 08:10:44 -05'00')

Capsule Fabrication

Component	Drawing	Rev.	Part	Material	Count	Comment	MAT IR	FAB IR	ID	Mass (g)
Holder Weldment	X3E020977A738	1	1	Al 6061	1		N/A	21194	CBH	4173.0500
Channel Box Internal Subassembly	X3E020977A765	1	1	N/A	1		N/A	N/A	CBOXInt	718.3411
									Total Mass	4891.3911

Experiment assembly fabrication request sheet.

Capsule Fabrication Request Sheet

Page 1 of 1
Date 3/3/2021

Target ID: CB01

Irradiation Conditions

Number cycles	2
First Cycle Goal	492
Assembly drawing	X3E020977A738 Rev.1

Approvals

	Request	Build
Performed by:	Annabelle Le Coq (Digitally signed by Annabelle Le Coq Date: 2021.03.03 11:48:00 -05'00')	David Bryant (Digitally signed by David Bryant Date: 2021.03.03 15:13:59 -05'00')
Checked by:	Christian M. Petrie (Digitally signed by Christian M. Petrie Date: 2021.03.03 13:26:27 -05'00')	Nicholas George Russell (Digitally signed by Nicholas George Russell Date: 2021.03.04 08:10:52 -05'00')

Capsule Fabrication

Component	Drawing	Rev.	Part	Material	Count	Comment	MAT IR	FAB IR	ID	Mass (g)
Pin	X3E020977A738	1	2	Al 6061	1		20962	20964	N/A	
Bottom cap	X3E020977A605	A	1	Al 6061	1		20957	20957	19-01	
EPRI Specimen Holder Upper Ring	X3E020977A605	A	3	Al 6061	1		20958	20958	19-01	4173.0500
Holder Half, A	X3E020977A739	1	1	Al 6061	1		20961	20961	N/A	
Holder Half, B	X3E020977A739	1	2	Al 6061	1		20961	20961	N/A	
									Total Mass	4173.0500

Experiment holder fabrication request sheet.

Capsule Fabrication Request Sheet

Page 1 of 1
Date 3/3/2021

Target ID: CB01

Irradiation Conditions

Number cycles	2
First Cycle Goal	492
Assembly drawing	X3E020977A765 Rev.1

Approvals

	Request	Build
Performed by:	Annabelle Le Coq (Digitally signed by Annabelle Le Coq Date: 2021.03.03 11:48:58 -05'00')	David Bryant (Digitally signed by David Bryant Date: 2021.03.03 15:14:23 -05'00')
Checked by:	Christian M. Petrie (Digitally signed by Christian M. Petrie Date: 2021.03.03 13:27:05 -05'00')	Nicholas George Russell (Digitally signed by Nicholas George Russell Date: 2021.03.04 08:11:02 -05'00')

Capsule Fabrication

Component	Drawing	Rev.	Part	Material	Count	Comment	MAT IR	FAB IR	ID	Mass (g)
Tie Rod	X3E020977A740	2	3	Al 6061	1		20960	20960	N/A	39.6009
Channel Box Specimen	X3E020977A740	2	4	SiC	1		21188	21188	CD	100.2936
Upper Box Support Weldment	X3E020977A764	1	1	Al 6061	1		N/A	N/A	UpBSW	239.7018
Lower Box Support Weldment	X3E020977A764	1	2	Al 6061	1		N/A	N/A	LowBSW	265.9176
Cladding Specimen	X3E020977A764	1	5	SiC	2		21195	21195	01	29.7997
									22	29.4967
Pin	X3E020977A764	1	4	Al 6061	4		20962	20963	N/A	1.3391
Hex nut, 2-56	90670A150	N/A		Al 6061	4	cage code:39428	21190	21190	N/A	0.2649
Wave spring	CS050-L4-S17	N/A		17-7 SS	8	cage code:51814	21189	21189	N/A	4.7731
Washer, 1/4"	91525A416	N/A		316 SS	1	cage code:39428	21191	21191	N/A	3.6427
Locknut, 1/4"-28	91853A515	N/A		18-8 SS	1	cage code:39428	21192	21192	N/A	3.2689
Cotter pin, 1/16" x 1/2" LG	98355A010	N/A		316 SS	1	cage code:39428	21193	21193	N/A	0.2421
									Total Mass	718.3411

Experiment internal fabrication request sheet.

Capsule Fabrication Request Sheet

Page 1 of 1
Date 3/3/2021

Target ID: CB01

Irradiation Conditions

Number cycles	2
First Cycle Goal	492
Assembly drawing	X3E020977A764 Rev.1

Approvals

	Request	Build
Performed by:	Annabelle Le Coq (Digitally signed by Annabelle Le Coq Date: 2021.03.03 11:51:27 -05'00')	David Bryant (Digitally signed by David Bryant Date: 2021.03.03 15:14:41 -05'00')
Checked by:	Christian M. Petrie (Digitally signed by Christian M. Petrie Date: 2021.03.03 13:27:55 -05'00')	Nicholas George Russell (Digitally signed by Nicholas George Russell Date: 2021.03.04 08:11:10 -05'00')

Capsule Fabrication

Component	Drawing	Rev.	Part	Material	Count	Comment	MAT IR	FAB IR	ID	Mass (g)
Box support, Lower	X3E020977A740	2	2	Al 6061	1		20959	20959	19-01	265.9176
Slotted pin	X3E020977A764	1	3	Al 6061	2		19728	19728	N/A	
									Total Mass	265.9176

Lower internal support fabrication request sheet.

Capsule Fabrication Request Sheet

Page 1 of 1
Date 3/3/2021

Target ID: CB01

Irradiation Conditions

Number cycles	2
First Cycle Goal	492
Assembly drawing	X3E020977A764 Rev.1

Approvals

	Request	Build
Performed by:	Annabelle Le Coq — Digitally signed by Annabelle Le Coq Date: 2021.03.03 11:50:28 -05'00'	David Bryant — Digitally signed by David Bryant Date: 2021.03.03 15:14:56 -05'00'
Checked by:	Christian M. Petrie — Digitally signed by Christian M. Petrie Date: 2021.03.03 13:27:27 -05'00'	Nicholas George Russell — Digitally signed by Nicholas George Russell Date: 2021.03.04 08:11:23 -05'00'

Capsule Fabrication

Component	Drawing	Rev.	Part	Material	Count	Comment	MAT IR	FAB IR	ID	Mass (g)
Box support, Upper	X3E020977A740	2	1	Al 6061	1		20959	20959	19-01	239.7018
Slotted pin	X3E020977A764	1	3	Al 6061	2		19728	19728	N/A	
									Total Mass	239.7018

Upper internal support fabrication request sheet.